

Generalized formulations producing a Burr distribution of speckle statistics

Kevin J. Parker^{a,*} and Sedigheh S. Pouli^b

^aUniversity of Rochester, Hajim School of Engineering and Applied Sciences, Department of Electrical and Computer Engineering, Rochester, New York, United States

^bUniversity of Rochester, Hajim School of Engineering and Applied Sciences, Department of Mechanical Engineering, Rochester, New York, United States

Abstract

Purpose: The study of speckle from imaging systems has a rich history, and recently it was proposed that a fractal or power law distribution of scatterers in vascularized tissue will lead to a form of the Burr probability distribution functions for speckle amplitudes. This hypothesis is generalized and tested in theory, simulations, and experiments.

Approach: We argue that two broadly applicable conjectures are sufficient to justify the applicability of the Burr distribution for speckle from a number of acoustical, optical, and other pulse-echo systems. The first requirement is a multiscale power law distribution of weak scatterers, and the second is a linear approximation for the increase in echo intensity with size over some range of applicability.

Results: The Burr distribution for speckle emerges under a wide variety of conditions and system parameters, and from this one can estimate the governing power law parameter, commonly in the range of 2 to 6. However, system effects including the imaging point spread function and the degree of focusing will influence the Burr parameters.

Conclusions: A generalized pair of conditions is sufficient for producing Burr distributions across a number of imaging systems. Simulations and some theoretical considerations indicate that the estimated Burr power law parameter will increase with increasing density of scatters. For studies of speckle from living tissue or multiscale natural structures, the Burr distribution should be considered as a long tail alternative to classical distributions.

© 2022 Society of Photo-Optical Instrumentation Engineers (SPIE) [DOI: [10.1117/1.JMI.9.2.023501](https://doi.org/10.1117/1.JMI.9.2.023501)]

Keywords: speckle; power law; fractal; backscatter; acoustics; optics.

Paper 21218R received Aug. 19, 2021; accepted for publication Jan. 31, 2022; published online Apr. 1, 2022.

1 Introduction

For more than 100 years, the random interference pattern from coherent illumination, which is called speckle, has been intensively studied. Originally, prisms were used in isolating narrow bands to investigate the phenomena in early work in light.¹ Even then, von Laue stated, “The theme of our investigation is an old one.” Studies of optical speckle intensified during the growth era of radar and lasers.^{2–8} Approximately 40 years ago, classical models were applied to speckle patterns in medical ultrasound.⁹ This work has significantly evolved and well-established statistical models now exist for the backscattered echoes from tissues.¹⁰

Over the past three decades, the study of ultrasound speckle from scatterers in normal (soft) tissue—and how the speckle changes in diseased tissue—has advanced, resulting in numerous models of ultrasound speckle. These advancements were influenced by prior work in the areas of electromagnetics. Specifically, the applied models include the following distributions and their

*Address all correspondence to Kevin J. Parker, kevin.parker@rochester.edu

closely related modifications: the Rayleigh,^{9,11–13} the K ,^{14–20} the Rician,^{6,21,22} the Nakagami,^{23–27} and the “marked model”^{28,29} as well as the comparison of distributions.^{30,31}

Other advanced models have been suggested,^{32,33} along with applications to a variety of clinical objectives.^{34–37}

A comprehensive review of speckle in acoustics including the key mathematical operations on probability density functions (PDFs) and distributions was recently published by Stanton et al.³⁸ This review also highlighted the interplay of the scattering types and their distributions with the beampattern used to illuminate the medium. More recently, a new hypothesis emphasizing weak scattering from tissue vasculature in medical ultrasound was developed.^{39–42} The scattering results were derived under the assumption that the branching vasculature can be modeled as a fractal branching set of cylinders. These were also considered to be a set of Born scatterers governed by a power law distribution of radii. This framework is separate from earlier work in a number of ways: the assumption of many identical scatterers contributing so as to approach the central limit theorem is replaced by consideration of few or individual scatterers, but those are distributed with a long tail distribution governed by a power law. This led to a surprising result—that ultrasound speckle amplitudes from tissue were plausibly modeled by a two-parameter Burr distribution, which was first formulated in the 1940s in the context of general functions for statistics research,⁴³ and to our knowledge was not been considered for speckle statistics. A key feature separating the Burr PDF from classical speckle models is its long power law tail. Some preliminary results from *in vivo* ultrasound have demonstrated the plausibility of the Burr PDF for medical ultrasound scans of the liver.^{40,42}

In this paper, we re-examine a more generalized set of conjectures, not limited to cylindrical models of the vasculature, but ultimately leading to distributions that are well approximated by the simple two-parameter Burr distribution. This implies that multiscale or fractal structures in medical ultrasound, underwater acoustics, optical coherence tomography (OCT), and possibly radar can be effectively studied or classified under a framework that emphasized power law behaviors and consequently a Burr distribution of speckle amplitudes.

2 Theory

2.1 Conjecture 1

Let the size distribution of any set of subresolved scatterers be given by a power law PDF of characteristic dimension a . In this context, subresolved scatterers are smaller than the resolution sample volume of the imaging system, so their exact shape and size are not resolved. Note that a power law PDF is consistent with a fractal distribution of scattering shapes,⁴⁴ which are found in many settings in the natural world.⁴⁵ The probability P of encountering or interrogating a scatterer of dimension a within the ensemble is given by

$$P(a) = \left(\frac{b-1}{a_{\min}} \right) \left(\frac{a_{\min}}{a} \right)^b, \quad (1)$$

where a_{\min} is some minimum value of dimension, and b is the key power law parameter governing the distribution of scattering size. For 3D fractal objects such as tree structures, b is typically found to be between 2 and 3.^{44,46} We assume that the multiscale nature of this distribution extends from small radii compared to the wavenumber k , where $k \cdot a_{\min} \ll 1$ (Rayleigh scattering) up to the resolution scale of the imaging system. Above this limit, targets begin to appear as discrete objects in broadband imaging systems and are typically excluded from the region of interest (ROI) analyzed as “speckle.”

2.2 Conjecture 2

The backscatter intensity from a plane wave of unit amplitude is assumed to be a linear function of a in the subresolved range, above some minimum level set by the system and by Rayleigh scattering lower limits. Consequently, the amplitude A is a square root mapping function:

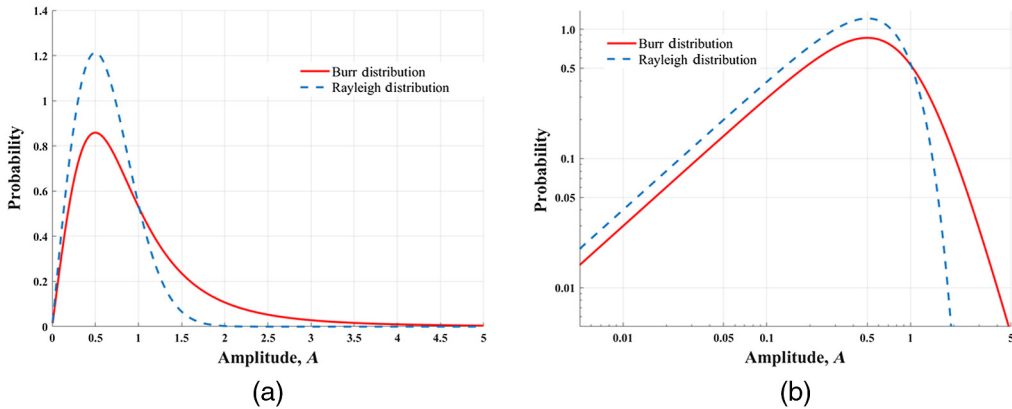


Fig. 1 The Burr PDF for scale factor $l = 1$ and power law $b = 2.5$, a typical value of b for 3D space-filling structures, compared with the Rayleigh distribution with the same mode value as the Burr distribution. (a) The Burr and Rayleigh PDFs are plotted in linear scale. (b) The same PDFs are shown in log–log scales.

$$A(a) = A_0 \sqrt{a - a_{\min}}. \quad (2)$$

To determine the probability of echo amplitude A given the probability distribution of scatterer size a , we apply the probability transformation mapping rule.^{38,42,47} Using the mapping function of Eq. (2) with the PDF of Eq. (1) directly yields the two-parameter Burr distribution,⁴²

$$\text{Burr } P(A) = \frac{2A(b-1)}{l^2 \left[\left(\frac{A}{l} \right)^2 + 1 \right]^b}, \quad (3)$$

where l is a scale factor and the range of validity is $A > 0$, $l > 0$ and $b > 1$. An example Burr distribution is shown in Fig. 1, both in linear and log–log plots, compared with the Rayleigh distribution (as the classical speckle distribution for random point scatterers), which has the same mode. The Rayleigh distribution appears more compact than the Burr distribution, highlighting the power law asymptotic behavior of the Burr distribution at higher amplitudes and, therefore, for larger scatterers.

The mean value of A is given by

$$\bar{A} = \frac{(-1+b)l\sqrt{\pi}\Gamma\left[-\frac{3}{2}+b\right]}{2\Gamma[b]} \text{ if } b > \frac{3}{2}. \quad (4)$$

Thus the mean or expected value of this distribution is proportional to the scale factor l , and for $b = 2.5$, which is typical for liver tissue, the mean is exactly equal to l .

Now let us re-examine conjecture 2, where we assume that the backscatter intensity from a plane wave of unit amplitude has a range where a first-order linear approximation can be employed. The general theory for backscattered intensity under the weak scattering or Born approximation would be k^4 times a form factor, which is related to the 3D spatial Fourier transform of the scattering shape or autocorrelation factor.^{48,49} Common treatments for discrete scatterers include spheres and cylinders. Furthermore, models for random media include Gaussian, modified Gaussian, exponential, and power law autocorrelation functions. Fractal structures, self-similar over a range of spatial scales, have a power law autocorrelation function.^{44,46} The backscattered intensity versus frequency trends for all these models are typically dominated by the k^4 behavior at long wavelengths (generally called Rayleigh scattering) and then leveling off as the influence of the form factor dominates when $ka > 1$ (the Mie scattering regime). Our first-order approximation generally applies to the transition region, between the ranges where the scattering is too weak to be captured in a limited dynamic range system with a noise floor, and at the other end where the object is so large as to be resolvable in imaging systems from the analysis

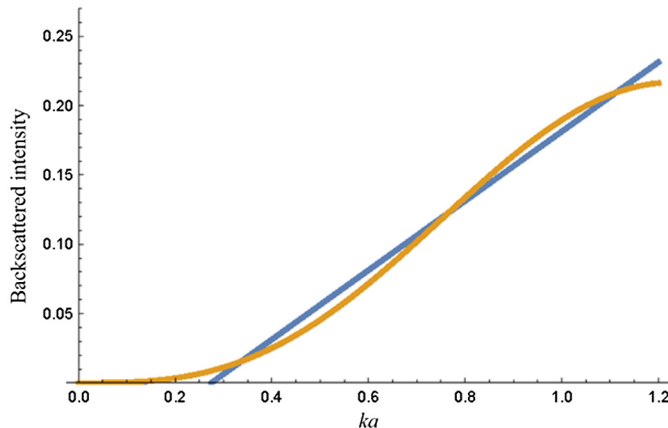


Fig. 2 Backscattered intensity (Born approximation or weak scattering) from a fluid sphere (blue) compared with a linear approximation covering the transition zone (orange) from approximately $ka = 0.2$ to 1.2 . Vertical axis is in arbitrary units, horizontal axis is dimensionless ka , wavenumber \times spherical radius.

of speckle. As an example, the classical solution for a weak spherical scatterer is examined, where the backscattered intensity is related to a spherical Bessel function (related to the 3D Fourier transform of a spherical shape) and is proportional to $k(ka)^3(j_1[2 ka]/(2 ka))^2$.^{48,50} This is shown in Fig. 2 along with a linear approximation in the transition zone, lying between the low ka region (Rayleigh scattering) and the Mies scattering region where $ka > 1$. The first-order approximation is a limited fit but captures a general relationship among the strongest scattering objects within the distribution of Eq. (1) and is consistent with a Taylor series expansion of a real function.⁵¹ Other general shapes, such as shells, Gaussian distributions,⁵⁰ and prolate spheroids⁵² possess similar trends, so the increasing scattering as a function of size, approximated as a first-order (linear) function over some limited range, can be seen to fit several models. Cylindrical scattering distributions have also been treated in this framework previously, both as isotropic distributions^{39,41} and considering only the perpendicular orientation.⁵³

2.3 Additional Factors: Beampattern Effects

The aforementioned conjectures lead directly to the Burr distribution, however, the simple probability transformation involving Eqs. (1) and (2), then Eq. (3) pertain to echoes considered individually from a uniform incident source irradiation. In the case of random location of small scatterers within a beampattern, one can formulate the ensemble of results as a product the random incident beam amplitude (formed by a random location within a prescribed beampattern) times the random scattering transfer function. The product rule for probability functions is used to derive the final, overall distribution of echoes.⁵⁴ This model is most appropriate for small scatterers within a broad unfocussed beampattern since the model tacitly assumes that each scatterer is exposed to a single value of incident wave amplitude within the beampattern. For the case of larger scatterers within a tightly focused beam, this assumption would be questionable, and so other forms of simulations or models are then required. However, considering larger scatterers within a tightly focused beam, this assumption would be questionable, and so other forms of simulations or models are then required.^{30,40,55} Specifically for OCT, a physics-based computational model encompassing system parameters has been developed.⁵⁵ This will be reconsidered in Secs. 3 and 4.

For the purpose of examining the product of probabilities model, let us assume the scatterers are sparse (noninteracting) within a circularly symmetric beampattern. The probability distribution for a random sampling point for conventional beampatterns has been shown to be in the form of a power law (see Appendix A of Ref. 54 and Sec. VII of Ref. 38) such that for a Gaussian, the beampattern PDF is proportional to $1/d$, where d is the amplitude within the beampattern, $d_{\min} < d < 1$ extending from some minimum value to a maximum of unity.

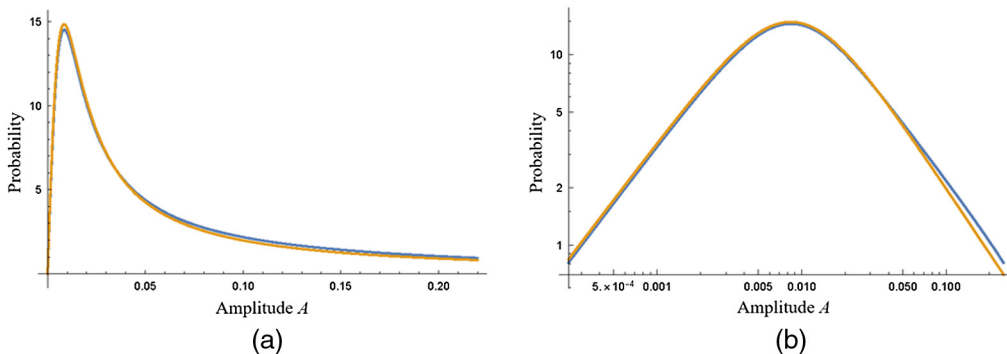


Fig. 3 Burr-in-Gaussian beampattern PDF for scale factor $l = 1$ and scatterer power law $b = 2.5$. (a) The resulting PDF is plotted in linear scale in blue, with a simple Burr distribution using $l = 0.009$ and $b = 1.07$ in orange, showing a reasonable match of the modified (in beampattern) to the theoretical Burr distributions. (b) The same two PDFs are shown in log–log scales.

Specifically for a Gaussian beampattern of amplitude $d_{\min} < d < 1$, the PDF of amplitude for a randomly located uniformly distributed scatterer is given by $\text{PDF} = -1/\log[d_{\min}d]$. Using the formula for the product of two independent random variables [Eq. (36b) from Ref. 38] and using x as the dummy variable of integration, we have⁵⁶

$$\begin{aligned} P(ec) &= \int_{d_{\min}}^1 \left(\frac{1}{x}\right) \left(\frac{-1}{\log[d_{\min}] \cdot x}\right) \left(\frac{2(b-1)\left(\frac{ec}{x}\right)}{l^2[(\frac{ec}{x}/l)^2 + 1]^b}\right) dx \\ &= \frac{\left(1 + \frac{ec^2}{l^2}\right)^{-b} (ec^2 + l^2) - \frac{\left(1 + \frac{ec^2}{l^2 d_{\min}^2}\right)^{-b} (ec^2 + l^2 d_{\min}^2)}{d_{\min}^2}}{ecl^2 \log[d_{\min}]} . \end{aligned} \quad (5)$$

This solution actually can be similar in shape to a Burr distribution but with a reduced scale and b parameter, as a result of the beampattern effects. An example is shown in Fig. 3.

2.4 Additional Factors: Summation of Multiple Scatterers Within the Resolution Cell

If two or more scatterers are included within the spatial resolution volume of a pulse-echo system, then a complex summation of their amplitudes is received, and the mathematics of phasor addition must be considered. When the phasors have PDFs, the summation of independent random variables is considered using convolution or related techniques (see Sec. IV of Ref. 38). The summation of Burr and related distributions leads to complicated series solutions,^{57–63} however for the case of two Burr phasors, we demonstrated that the leading term contained a higher power law of $b + 1/2$, increasing for additional phasors.⁴² Practically speaking, this means that higher numbers of scatterers per sample volume will produce echo PDFs where the estimate of Burr b parameter will exceed the inherent b of Eq. (1). In general, as the number of scatterers exceeds eight,^{28,29} the statistical result will approach the central limit theorem, leading to a Rayleigh PDF in amplitude,⁶⁴ however, the convergence of heavy-tailed power law distributions is notoriously slow, and in many applications with high-resolution imaging configurations we anticipate only a few scatterers per sample volume.

In summary, there are numerous imaging system effects that can influence the reflections from natural fractal structures. Importantly, in highly focused imaging beampatterns, some scatterers in Eq. (1) will become large with respect to the beampattern, rendering the derivation of Eq. (5) as an oversimplification. Also the number of scatterers within an imaging point spread function, along with practical limits on scatterer sizes, will modify results. With these issues in mind, some simulations are examined next for comparison.

3 Methods

To numerically study the relationships of the scatterer distributions with the resulting speckle statistics and the underlying statistical Burr parameters, a series of 3D simulations are performed using the *k*-Wave toolbox in MATLAB (The Mathworks, Inc., Natick, MA, USA).^{53,65} Here we focus on sets of simulation cases with different scatterer distributions that all mutually obey the power law behavior with the scatterers' radii. The background material has a speed of sound of $c = 1540$ m/s and with a low attenuation of 0.004 dB/cm/MHz to simplify the comparison across different depths. The scatterers are all modeled as spherical in shape with different radii whose surfaces are randomly rounded to the nearest quantized voxel to avoid artificially flat (quantized) surfaces, and their spatial distributions are also random within the 3D background medium, which is considered as the tissue parenchyma. These spherical scatterers are considered as inhomogeneous regions with material properties $\sim 3\%$ different than the background medium to have an impedance difference for the acoustic reflections. Consistent with conjecture 1 and Eq. (1), the number densities of spherical scatterers with different radii are modeled to obey a power law relationship as $N(r) = N_0/r^b$, where N_0 corresponds to the number of scatterers with unit radius placed randomly within the simulation volume and r is the radius in units of discrete spherical scatterers. The range of r extends in the simulation from 0.5 to 6 elements, thus the largest sphere is of diameter 12 elements, or ~ 0.83 mm and the smallest scatterer is ~ 0.07 mm. These spheres can be seen in Fig. 4. The power law distribution on the scatterers' number density is governed by the power law parameter b , which is set in the range of 2 to 3 in this study to mimic the physiological range. In this study, 15 different simulations based on changes in the values of b (2.2, 2.5, 2.8) and N_0 (1000, 1500, 2500, 3500, 4500) are implemented to investigate cases with different scatterer distributions.

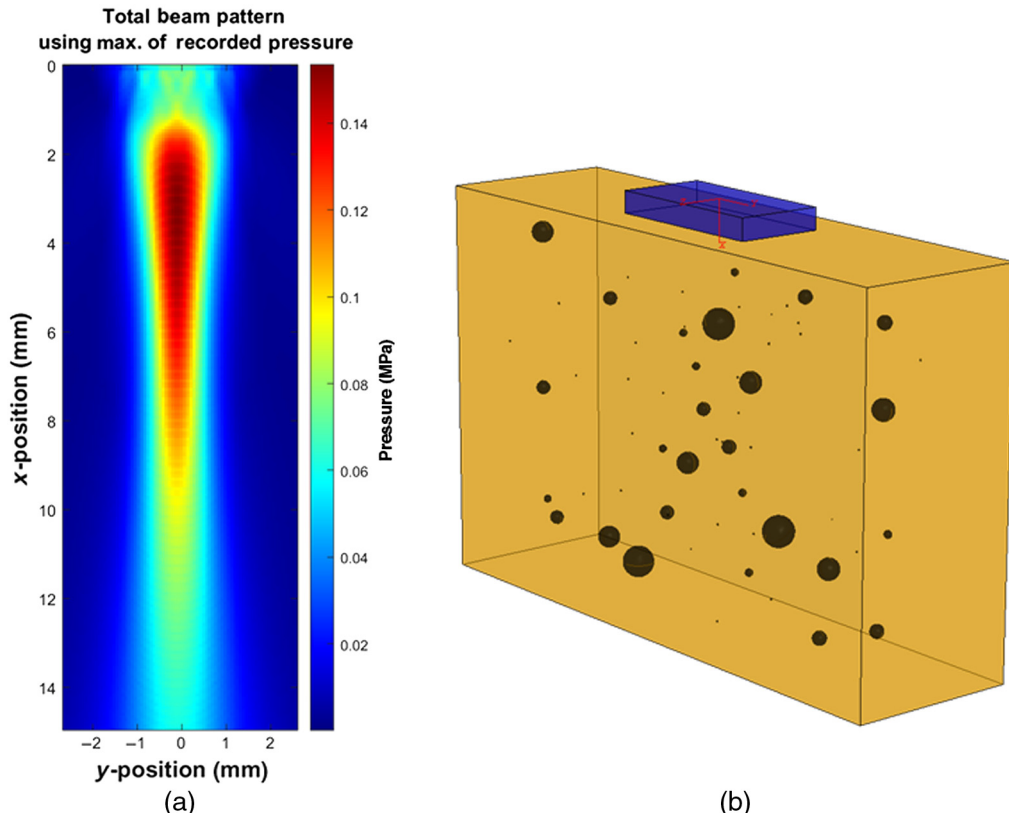


Fig. 4 (a) The beampattern of the linear array transducer. (b) The schematic of the 3D view of the medium showing some spherical scatterers with different densities distributed in a uniform background. The transducer orientation is also shown on top of the domain as a small blue rectangular box.

The dimensions of the 3D domain are 15 mm along depth, 13 mm along the lateral direction, and 3 mm along the transverse direction. The mesh sizes along the three dimensions are uniform with the element size of ~ 0.069 mm in all three directions. The computational time step is $\sim 1.3 \times 10^{-8}$ s, consistent with the Courant–Friedrichs–Lowy (CFL) criteria, which require a CFL number $\text{CFL} = (c_0 \Delta t / \Delta x) \leq 0.3$ to enable a stable simulation.

A linear array transducer model is implemented in *k*-Wave for this study. The transducer is excited by a two-cycle toneburst signal with the frequency of 4 MHz. The transducer wavelength at center frequency is 0.385 mm. This frequency is close to the common range of frequencies set for the abdominal scan in adult human populations. In order to reduce the side lobe artifacts, the transducer element width is set to the value less than the half of the wavelength. Also to minimize the reflection artifact from the waves reflecting back to the medium after interacting with the boundaries, an absorbing layer called a perfectly matched layer is implemented around the 3D medium that absorbs the pressure waves.

The B-scans of the scattering media are reconstructed by implementing beamforming, frequency filtering, envelope detection, and compression of the radio frequency data from the simulations. The PDF of the envelope of echo amplitudes is then calculated for an appropriate ROI and fitted to the Burr distribution using the nonlinear least squared method implemented in MATLAB.

4 Results

4.1 Ultrasound

The transducer beam pattern is shown in Fig. 4(a) using the recorded pressure field. The near-zone (Fresnel) region, the focal region, as well as the far (Fraunhofer) zone are observed from this figure. A schematic 3D view of the scattering medium is presented in Fig. 4(b) incorporating a few spherical scatterers with different diameters distributed randomly within the background material. The transducer orientation with respect to the medium is also shown on top of the 3D domain as a small blue rectangular box.

Initially, we investigate how the echo intensities increase with scatterers' radii. To do so, we evaluate separate realizations of a single scatterer with a specific radius. In addition, we consider individual scatterers in the medium located at different depths, ~ 5.0 , 7.5, and 10 mm to vary the echo with respect to the nominal focus of ~ 10 mm.

First, the spatially averaged echo intensities coming from each scatterer at a specific depth are obtained, and then the mean of these averaged intensity measurements from these three single-radius scatterers is calculated. This process is independently repeated for different radii and the results are shown in Fig. 5. As observed, the average intensity increases with the scatterer radius and the underlying correlation between intensity and radius is approximated reasonably as a linear relationship. This is well-consistent with our earlier assumptions in modeling intensity versus radius in conjecture 2. Variations are due to the different depths simulated and to the random roughness of the spheres around the quantized voxel sizes used in the simulation. Note that the results of Fig. 5 are consistent with the general trend of Fig. 2, however, that is a different calculation related to backscatter from a monochromatic plane wave. Figure 5 represents received echo intensity from a focused broadband system. These concepts are related but not identical, as system effects play a major role in defining the outcomes of Fig. 5.

Figure 6 shows the 2D (*x*-*y*) view of the middle plane cut through four different 3D scattering structures, in which the numbers and sizes of scatterers follow a power law function characterized by two different parameters: *b* and N_0 . These four cases with different scatterer densities correspond to high and low values of *b* and N_0 in this study. The black regions represent the scatterers with different diameters distributed in a homogeneous background media. Figures 6(a) and 6(b) show two samples from the category with the power law parameter of *b* = 2.8, and Figs. 6(c) and 6(d) show for the category with *b* = 2.2, both for the cases of N_0 = 4500 and N_0 = 1000.

Comparing these scatterer density cases, it is observed that for a constant N_0 , when *b* is smaller, the number density of the random scatterers with a specific diameter is higher than for

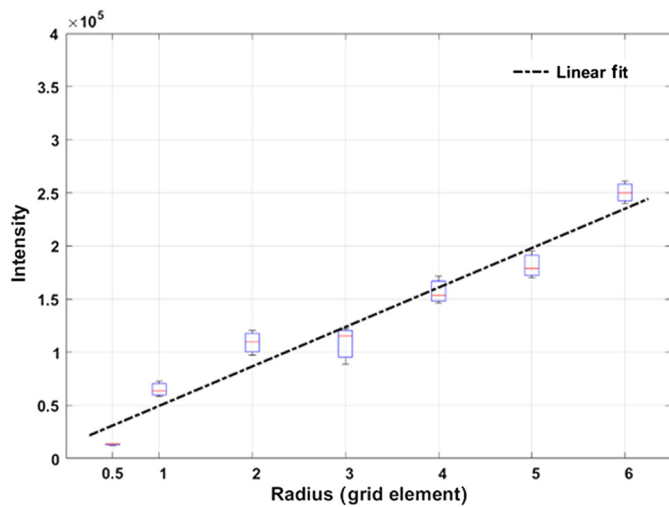


Fig. 5 Spatially averaged echo intensity as a function of scatterer radii along with the linear correlation fit. Boxplots show intensity variations across three different realizations repeated for each radius.

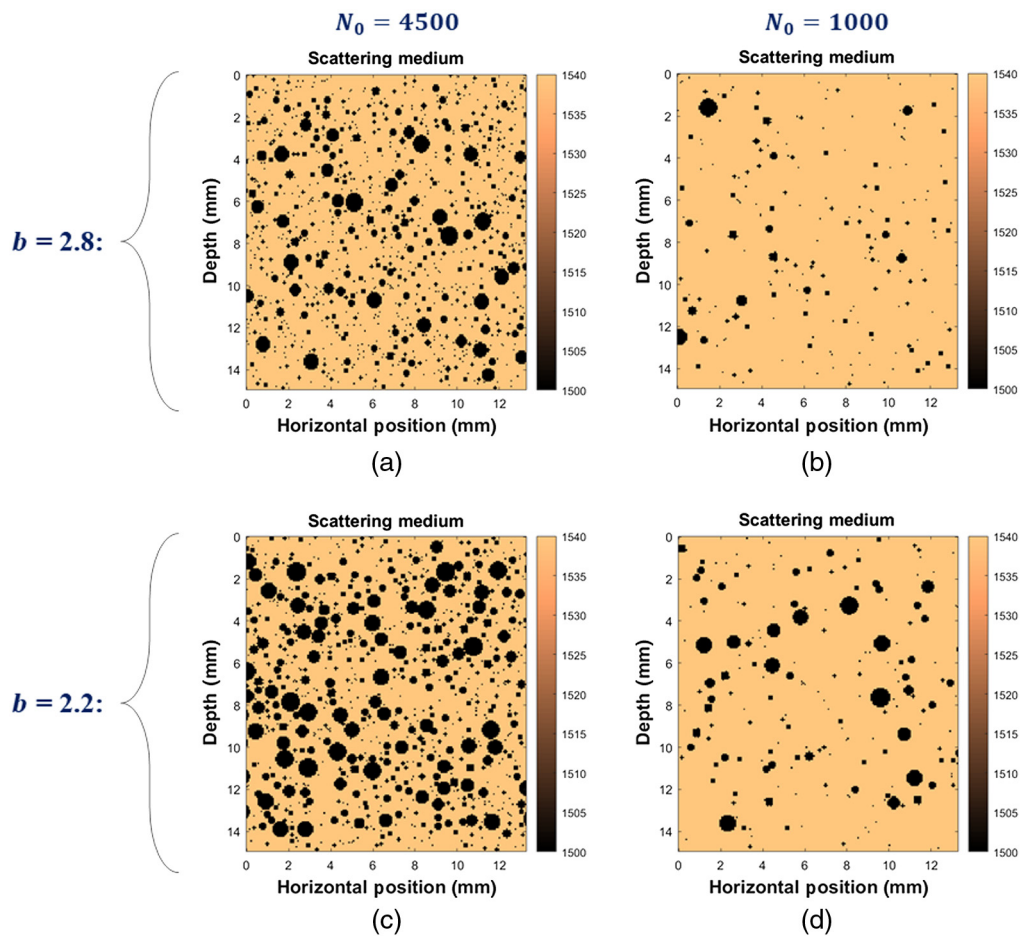


Fig. 6 The 2D plane cut through the middle of four different 3D scattering media corresponding to the power law parameter of $b = 2.8$ when (a) $N_0 = 4500$ and (b) $N_0 = 1000$, and to the power law parameter of $b = 2.2$ when (c) $N_0 = 4500$ and (d) $N_0 = 1000$.

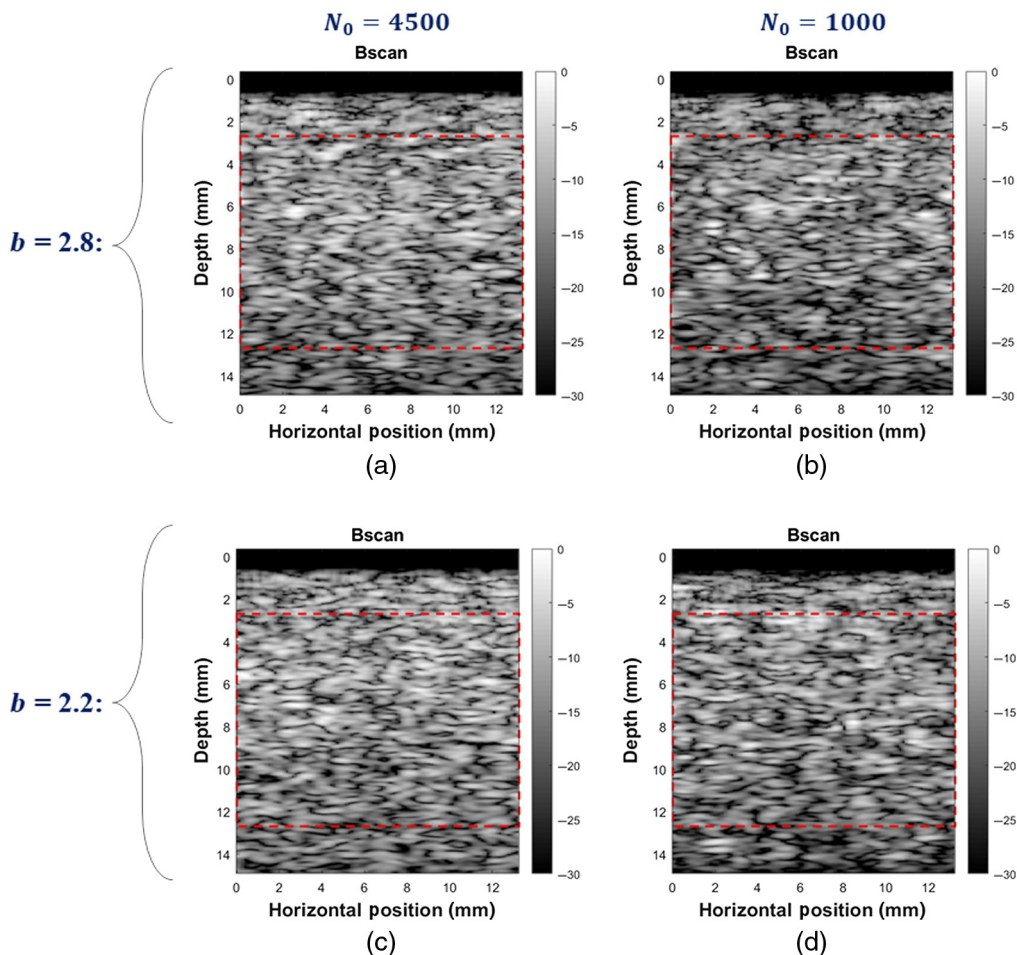


Fig. 7 The B-scan images corresponding to the scattering structures with the power law parameter of $b = 2.8$ when (a) $N_0 = 4500$ and (b) $N_0 = 1000$, and for the scattering medium with the power law parameter of $b = 2.2$ when (c) $N_0 = 4500$ and (d) $N_0 = 1000$.

cases with larger b . The corresponding B-scan images for the four scattering media in Fig. 6 are shown in Fig. 7. The ROIs for obtaining the speckle statistics of echoes are depicted as a red rectangular region on each B-scan.

Figure 8 demonstrates the details of the speckle statistics for the four cases shown in Fig. 7. This figure presents the speckle statistics data obtained from a large ROI on the B-scan, as well as the curves from fitting the Burr distribution to the speckle statistics data. The histogram for each case is presented in two forms: (i) linear-binned axes and (ii) log-binned axes. The latter representation allows us to examine how the speckle data behaves around the initial and final tails of the distribution. Therefore, we can assure that the fitted curves from the Burr distribution are capturing the overall details of the speckle data. In Fig. 8, it is observed that the fitted curve for each case shows close agreement with the speckle data from the simulations, and this indicates that the Burr distribution is capable of capturing the speckle statistics for the scatterers distributed according to the power law relationship. The fitting parameters of the Burr distribution for these four cases are presented in Table 1. The average number of scatterers per unit volume of the interrogating pulse for each case is also presented in Table 1. For this calculation, the pulse volume is approximated as an 8-dB ellipsoid in 3D averaged over echoes from three single voxel scatterers at different depths. The higher numbers of scatterers per pulse volume are associated with significant complex summations of amplitudes within the acoustic pulse and explain the elevated values for \hat{b} obtained from the histograms. It should be noted that the power law parameter used to create the spherical scattering structures is called the generating power law parameter

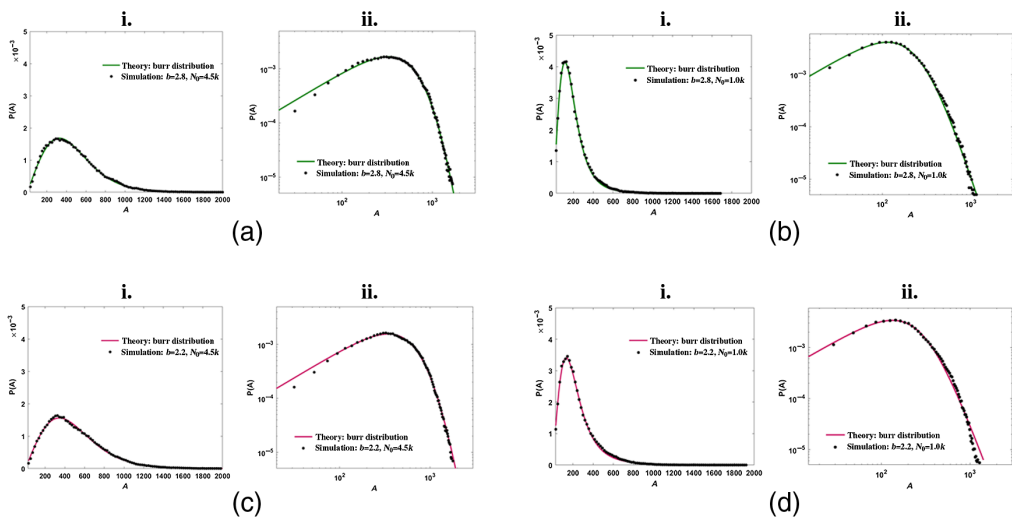


Fig. 8 The speckle statistics data shown as: (i) linear-binned scale and (ii) log-binned scale for the power law scatterer distributions with (a) $b = 2.8$, $N_0 = 4500$; (b) $b = 2.8$, $N_0 = 1000$; (c) $b = 2.2$, $N_0 = 4500$; and (d) $b = 2.2$, $N_0 = 1000$. The Burr-fitted curves to the speckle data are also shown in each case as a solid line.

Table 1 Four samples of the results from fitting the Burr distribution to the speckle statistics for the cases shown in Fig. 8. The last column shows the number of scatterers per unit of pulse volume.

Scattering case	Fitting results			Approximate number of scatterers per unit pulse volume
	\hat{b}	I	R^2	
(a) $b = 2.8$, $N_0 = 4500$	7.01	1179.16	0.9975	6.3
(b) $b = 2.8$, $N_0 = 1000$	3.16	263.80	0.9985	1.4
(c) $b = 2.2$, $N_0 = 4500$	5.90	1132.60	0.9974	4.6
(d) $b = 2.2$, $N_0 = 1000$	2.87	289.50	0.9981	1.0

here and is shown as b , whereas the parameter obtained from fitting the Burr distribution to the speckle data is indicated as \hat{b} and is called the fitted (or estimated) power law parameter.

To summarize the results from all the simulations across different N_0 and different b , which both play a role in the scatterer densities, the fitting results of the speckle statistics for the Burr power law parameters are shown in Fig. 9. The results indicate that the fitted power law parameter \hat{b} is a sensitive parameter that changes with the scatterer distribution: either a change in the generating power law parameter response to any variation in b or a change in N_0 . It is observed that \hat{b} increases by increasing N_0 and also b . In order to assess the variability in estimating \hat{b} from different realizations of random scatterer distributions, for two scattering cases of ($b = 2.8$ and $N_0 = 2500$) and ($b = 2.2$ and $N_0 = 2500$), we simulated five independent realizations for each case and reported the mean and standard deviation of the fitting parameter in the form of error bars shown in Fig. 9.

4.2 Optical Coherence Tomography

Following the methods of Ge et al.,⁶⁶ results from OCT studies of fresh samples of calf liver were examined for speckle statistics. The scanning system utilized a swept source laser (HSL-2100-WR, Santec, Aichi, Japan) with a center wavelength of 1310 nm and full-width half-maximum

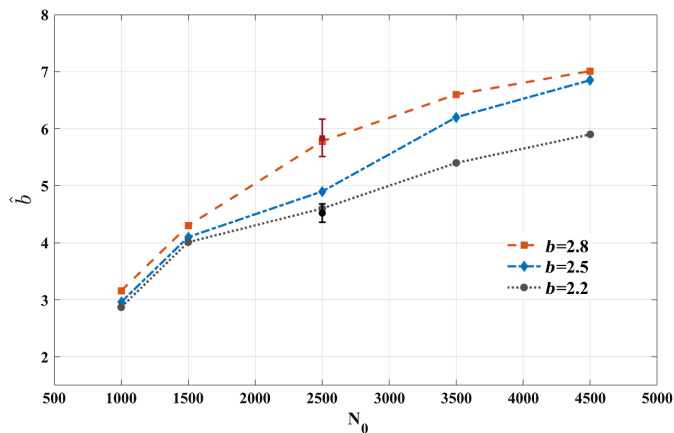


Fig. 9 The summary of the results from fitting the Burr distribution to the speckle statistics data for all 15 simulation cases. The two error bars represent the means and standard deviations of the fitting parameter \hat{b} obtained from five different realizations repeated for the simulation cases ($\{b = 2.8, N_0 = 2500\}$ and $\{b = 2.2, N_0 = 2500\}$).

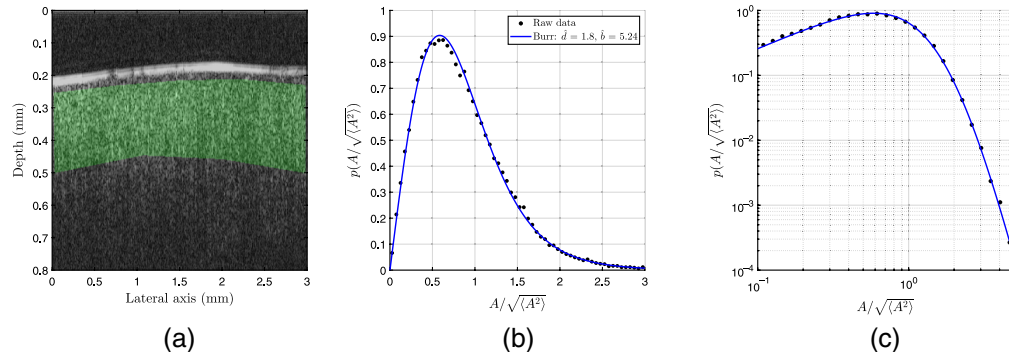


Fig. 10 Optical coherence tomography scan of a fresh calf liver, *ex vivo*, is shown in (a). The liver surface is a bright horizontal line, the speckle below is analyzed for amplitude statistics, with the ROI shown in green. The histogram of amplitudes is shown below in (b) linear and (c) log–log formats with a mean squared error best fit to a Burr distribution with an estimated \hat{b} of 5.2.

bandwidth of 170 nm. The liver specimen was cut using a surgical knife from a freshly obtained calf liver and selected to be free of major arteries, connective tissue, and the outer capsule. The OCT scan and Burr best fit histograms are shown in Figs. 10(a)–10(c). Similar to the OCT results from other tissues reported in Ge et al.,⁶⁶ the speckle statistics are effectively characterized by the Burr distribution with an estimated b in the range found in other soft vascularized tissues.

4.3 Radar and Sonar of Vegetation

We do not currently have available raw echo amplitude distributions from plausibly fractal vegetation scattering targets using radar or sonar systems. However, we note that in early studies of radar crop analysis,⁶⁷ some heavy-tail distributions were noted. These heavy-tails are not consistent with Rayleigh distributions but could be more consistent with Burr and other power law PDFs. Similarly, in some sonar studies,^{68–70} some heavy-tail distributions were noted, leading to a better fit using the generalized Pareto or mixture distributions over earlier Rayleigh and exponential models. It remains to be seen if the Burr distribution can effectively capture the long tail distributions formed in these cases.

5 Discussion and Conclusion

We propose two simple conjectures that are sufficient to produce a Burr distribution of echo amplitudes. First, scatterers are distributed according to a power law with respect to size (consistent with fractal and multiscale structures), and second, their echo intensity increases with size as a first-order approximation over some range in the subresolved region. Together, these two conjectures predict the emergence of speckle PDFs that are modeled by a Burr distribution determined by a scale parameter and a governing power law b . These conjectures are somewhat general and not restricted to perfect spheres or cylinders. This Burr model of speckle amplitudes is expected to be useful in situations where multiscale or fractal distribution of scatterers is present. In addition, for experimental studies of speckle, the Burr PDF uniquely provides a long-tail, power law asymptote, which is distinct from classical models. The Burr parameters have shown promise for differentiating different tissue types and pathological states in preliminary studies in OCT⁶⁶ and ultrasound.^{40,42,71} This model would not be relevant in situations where organized structures, periodic targets, or large numbers of scatterers are interrogated. In practical situations, there are a number of additional system factors that influence the speckle statistics; we considered only a few aspects of the effects of beampatterns and the effects of the number of scatterers per unit volume.

Limitations of this work include the need for additional analysis of raw data from different sources that image multiscale weak scatterers. Although we have access to ultrasound and OCT data,^{42,66,72} we do not currently have examples from radar and sonar. The derivations also do not include the effects of attenuation, or multiple scattering which would be influential in a number of situations. It remains to be seen how effectively the inherent power law parameter b can be deduced from measurements of the estimated \hat{b} . Finally, the effect of the beampattern for cases where the scattering objects are comparable to the beampattern has not been fully explored in theory, although we have presented simulations and convolutional models to provide examples.

In summary, we postulate that the Burr distribution can be a meaningful model across a wide set of applications in ultrasound, optics, radar, and sonar where weak multiscale natural scatterers are interrogated by imaging systems. The two Burr parameters may be useful in characterizing the targets, however, further research is required to make these more rigorously system independent.

Disclosures

The authors have no relevant financial interests in the manuscript and no other potential conflicts of interest to disclose.

Acknowledgments

This work was support by the National Institutes of Health Grant Nos. R21EB025290 and R21AG070331. The authors would like to thank Gary R. Ge, MD/PhD candidate at the University of Rochester, for providing the OCT scans and data analysis of the calf liver. We were grateful for many insightful comments and key references from Professor T. K. Stanton.

References

1. M. von Laue, Translated by H. K. V. Lotsch, “Sitzungsberichte der Koenig,” *Pruess Akad Wiss* **47**, 1144 (1914).
2. N. George and A. Jain, “Speckle in microscopy,” *Opt. Commun.* **6**(3), 253–257 (1972).
3. N. George and A. Jain, “The wavelength diversity of speckle,” *Proc. SPIE* **0041**, 161–167 (1974).
4. N. George and A. Jain, “Space and wavelength dependence of speckle intensity,” *Appl. Phys.* **4**(3), 201–212 (1974).

5. N. George, A. Jain, and R. D. S. Melville, "Speckle, diffusers, and depolarization," *Appl. Phys.* **6**(1), 65–70 (1975).
6. J. W. Goodman, "Statistical properties of laser speckle patterns," in *Laser Speckle and Related Phenomenon*, J. C. Dainty, Ed., pp. 9–75, Springer-Verlag, Heidelberg (1975).
7. J. W. Goodman, "Some fundamental properties of speckle," *J. Opt. Soc. Am.* **66**(11), 1145–1150 (1976).
8. N. George and D. C. Sinclair, "Editor's page: topical issue on laser speckle," *J. Opt. Soc. Am.* **66**(11), 1316–1316 (1976).
9. C. B. Burckhardt, "Speckle in ultrasound b-mode scans," *IEEE Trans. Son. Ultrason.* **25**(1), 1–6 (1978).
10. J. M. Thijssen, "Ultrasonic speckle formation, analysis and processing applied to tissue characterization," *Pattern Recognit. Lett.* **24**(4), 659–675 (2003).
11. R. F. Wagner et al., "Statistics of speckle in ultrasound b-scans," *IEEE Trans. Son. Ultrason.* **30**(3), 156–163 (1983).
12. B. J. Oosterveld, J. M. Thijssen, and W. A. Verhoef, "Texture of B-mode echograms: 3-D simulations and experiments of the effects of diffraction and scatterer density," *Ultrason. Imaging* **7**(2), 142–160 (1985).
13. K. A. Wear et al., "Statistical properties of estimates of signal-to-noise ratio and number of scatterers per resolution cell," *J. Acoust. Soc. Am.* **102**(1), 635–641 (1997).
14. E. Jakeman and R. J. A. Tough, "Generalized K distribution: a statistical model for weak scattering," *J. Opt. Soc. Am. A* **4**(9), 1764–1772 (1987).
15. G. E. Sleefe and P. P. Lele, "Tissue characterization based on scatterer number density estimation," *IEEE Trans. Ultrason. Ferroelectr. Freq. Control* **35**(6), 749–757 (1988).
16. V. Dutt and J. F. Greenleaf, "Speckle analysis using signal to noise ratios based on fractional order moments," *Ultrason. Imaging* **17**(4), 251–268 (1995).
17. R. C. Molthen et al., "Comparisons of the Rayleigh and K-distribution models using in vivo breast and liver tissue," *Ultrasound Med. Biol.* **24**(1), 93–100 (1998).
18. Y. W. Tsai et al., "Ultrasound detection of liver fibrosis in individuals with hepatic steatosis using the homodyned K distribution," *Ultrasound Med. Biol.* **47**(1), 84–94 (2021).
19. Z. Zhou et al., "Value of homodyned K distribution in ultrasound parametric imaging of hepatic steatosis: an animal study," *Ultrasonics* **101**, 106001 (2020).
20. G. Ghoshal et al., "Ex vivo study of quantitative ultrasound parameters in fatty rabbit livers," *Ultrasound Med. Biol.* **38**(12), 2238–2248 (2012).
21. M. F. Insana et al., "Analysis of ultrasound image texture via generalized Rician statistics," *Opt. Eng.* **25**(6), 256743 (1986).
22. J. M. Thijssen, "Echographic image processing," in *Advances in Electronics and Electron Physics*, P. W. Hawkins, Ed., pp. 317–349, Academic Press, Boston, Massachusetts (1992).
23. P. M. Shankar, "Ultrasonic tissue characterization using a generalized Nakagami model," *IEEE Trans. Ultrason. Ferroelectr. Freq. Control* **48**(6), 1716–1720 (2001).
24. P. M. Shankar, "A compound scattering pdf for the ultrasonic echo envelope and its relationship to K and Nakagami distributions," *IEEE Trans. Ultrason. Ferroelectr. Freq. Control* **50**(3), 339–343 (2003).
25. Z. Zhou et al., "Hepatic steatosis assessment with ultrasound small-window entropy imaging," *Ultrasound Med. Biol.* **44**(7), 1327–1340 (2018).
26. P. H. Tsui et al., "Acoustic structure quantification by using ultrasound Nakagami imaging for assessing liver fibrosis," *Sci. Rep.* **6**, 33075 (2016).
27. F. Fang et al., "Ultrasound assessment of hepatic steatosis by using the double Nakagami distribution: a feasibility study," *Diagnostics (Basel)* **10**(8), 557 (2020).
28. R. M. Cramblitt and K. J. Parker, "Generation of non-Rayleigh speckle distributions using marked regularity models," *IEEE Trans. Ultrason. Ferroelectr. Freq. Control* **46**(4), 867–874 (1999).
29. T. A. Tuthill, R. H. Sperry, and K. J. Parker, "Deviations from Rayleigh statistics in ultrasonic speckle," *Ultrason. Imaging* **10**(2), 81–89 (1988).
30. E. Hysi et al., "Insights into photoacoustic speckle and applications in tumor characterization," *Photoacoustics* **14**, 37–48 (2019).

31. Z. Zhou et al., "Hepatic steatosis assessment using quantitative ultrasound parametric imaging based on backscatter envelope statistics," *Appl. Sci.* **9**(4), 661 (2019).
32. R. W. Prager et al., "Analysis of speckle in ultrasound images using fractional order statistics and the homodyned k-distribution," *Ultrasonics* **40**(1-8), 133–137 (2002).
33. T. Yamaguchi, "The quantitative ultrasound diagnosis of liver fibrosis using statistical analysis of the echo envelope," Chapter 11 in *Quantitative Ultrasound in Soft Tissues*, J. Mamou and M. L. Oelze, Eds., pp. 275–288, Springer Netherlands, Dordrecht (2013).
34. F. Destrempe and G. Cloutier, "A critical review and uniformized representation of statistical distributions modeling the ultrasound echo envelope," *Ultrasound Med. Biol.* **36**(7), 1037–1051 (2010).
35. Z. Klimonda et al., "Ultrasound scattering statistics predicts the result of neoadjuvant chemotherapy of breast tumors at an early stage of treatment," in *IEEE Int. Ultrason. Symp. (IUS)*, pp. 1512–1514 (2019).
36. A. Tang et al., "Quantitative ultrasound and machine learning for assessment of steatohepatitis in a rat model," *Eur. Radiol.* **29**(5), 2175–2184 (2019).
37. R. Hu et al., "Acoustic shadow detection: study and statistics of B-mode and radiofrequency data," *Ultrasound Med. Biol.* **45**(8), 2248–2257 (2019).
38. T. K. Stanton, W. Lee, and K. Baik, "Echo statistics associated with discrete scatterers: a tutorial on physics-based methods," *J. Acoust. Soc. Am.* **144**(6), 3124–3171 (2018).
39. K. J. Parker, J. J. Carroll-Nellenback, and R. W. Wood, "The 3D spatial autocorrelation of the branching fractal vasculature," *Acoustics* **1**(2), 369–381 (2019).
40. K. J. Parker, "The first order statistics of backscatter from the fractal branching vasculature," *J. Acoust. Soc. Am.* **146**(5), 3318–3326 (2019).
41. K. J. Parker, "Shapes and distributions of soft tissue scatterers," *Phys. Med. Biol.* **64**(17), 175022 (2019).
42. K. J. Parker and S. S. Poul, "Burr, Lomax, Pareto, and logistic distributions from ultrasound speckle," *Ultrason. Imaging* **42**(4-5), 203–212 (2020).
43. I. W. Burr, "Cumulative frequency functions," *Ann. Math. Stat.* **13**(2), 215–232 (1942).
44. T. Vicsek, *Fractal Growth Phenomena*, 2nd. ed., World Scientific, Singapore (1992).
45. B. B. Mandelbrot, *Fractals : Form, Chance, and Dimension*, W.H. Freeman, San Francisco (1977).
46. J. J. Carroll-Nellenback et al., "Liver backscatter and the hepatic vasculature's autocorrelation function," *Acoustics* **2**(1), 3–12 (2020).
47. A. Papoulis, *Probability, Random Variables, and Stochastic Processes*, McGraw-Hill, New York (1965).
48. L. Rayleigh, "On the scattering of light spherical shells, and by complete spheres of periodic structure, when the refractivity is small," *Proc. R. Soc. Lond. Ser. A* **94**(660), 296–300 (1918).
49. P. M. Morse and K. U. Ingard, *Theoretical Acoustics*, Princeton University Press, Princeton, New Jersey (1987).
50. M. F. Insana et al., "Describing small-scale structure in random media using pulse-echo ultrasound," *J. Acoust. Soc. Am.* **87**(1), 179–192 (1990).
51. M. Abramowitz and I. A. Stegun, *Handbook of Mathematical Functions with Formulas, Graphs, and Mathematical Tables*, US Government Printing Office (1970).
52. R. Spence and S. Granger, "The scattering of sound from a prolate spheroid," *J. Acoust. Soc. Am.* **23**(6), 701–706 (1951).
53. K. J. Parker and S. S. Poul, "Speckle from branching vasculature: dependence on number density," *J. Med. Imaging* **7**(2), 027001 (2020).
54. J. E. Ehrenberg et al., "Indirect measurement of the mean acoustic backscattering cross section of fish," *J. Acoust. Soc. Am.* **69**(4), 955–962 (1981).
55. V. Y. Zaitsev et al., "A model for simulating speckle-pattern evolution based on close to reality procedures used in spectral-domain OCT," *Laser Phys. Lett.* **11**(10), 105601 (2014).
56. T. K. Stanton, "This equation was originally derived by T. K. Stanton in a different form; personal communication with K. J. Parker in March," (2021).
57. M. H. Tahir et al., "The Weibull-Lomax distribution: properties and applications," *Hacet. J. Math. Stat.* **44**(2), 455–474 (2015).

58. N. Balakrishnan, *Handbook of the Logistic Distribution*, Dekker, New York (1992).
59. S. Nadarajah, “Exponentiated Pareto distributions,” *Statistics* **39**(3), 255–260 (2005).
60. S. Nadarajah and M. M. Ali, “Pareto random variables for hydrological modeling,” *Water Resour. Man* **22**(10), 1381–1393 (2008).
61. S. Nadarajah, “Exact distribution of the product of m gamma and n Pareto random variables,” *J. Comput. Appl. Math.* **235**(15), 4496–4512 (2011).
62. Q. H. Nguyen and C. Robert, “Series expansions for sums of independent Pareto random variables,” Lyon (2013).
63. W. Abu-Dayyeh, A. Assrhani, and K. Ibrahim, “Estimation of the shape and scale parameters of Pareto distribution using ranked set sampling,” *Stat. Pap.* **54**(1), 207–225 (2013).
64. D. Middleton, *An Introduction to Statistical Communication Theory*, McGraw-Hill, New York, (1960).
65. B. E. Treeby et al., “Modelling elastic wave propagation using the k-Wave MATLAB Toolbox,” in *IEEE Int. Ultrason. Symp.*, pp. 146–149 (2014).
66. R. G. Ge, J. P. Rolland, and K. J. Parker, “Speckle statistics of biological tissues in optical coherence tomography,” *Biomed. Opt. Express* **12**(7), 4179–4191 (2021).
67. K. R. Menon et al., “Characterization of fluctuation statistics of radar clutter for Indian terrain,” *IEEE Trans. Geosci. Remote Sens.* **33**(2), 317–324 (1995).
68. J. M. Gelb, R. E. Heath, and G. L. Tipple, “Statistics of distinct clutter classes in midfrequency active sonar,” *IEEE J. Ocean. Eng.* **35**(2), 220–229 (2010).
69. D. A. Abraham, J. M. Gelb, and A. W. Oldag, “Background and clutter mixture distributions for active sonar statistics,” *IEEE J. Ocean. Eng.* **36**(2), 231–247 (2011).
70. T. K. Stanton et al., “Interpreting echo statistics of three distinct clutter classes measured with a midfrequency active sonar: accounting for number of scatterers, scattering statistics, and Bbeam pattern effects,” *IEEE J. Ocean. Eng.* **40**(3), 657–665 (2015).
71. J. Baek et al., “Scattering signatures of normal versus abnormal livers with support vector machine classification,” *Ultrasound Med. Biol.* **46**(12), 3379–3392 (2020).
72. M. Niemczyk and D. R. Iskander, “Statistical analysis of corneal OCT speckle: a non-parametric approach,” *Biomed. Opt. Express* **12**(10), 6407–6421 (2021).

Kevin J. Parker is the William F. May Professor of Engineering at the University of Rochester. He received his graduate degrees from Massachusetts Institute of Technology and served at the University of Rochester as Department Chair, Director of the Rochester Center for Biomedical Ultrasound, and Dean of the Hajim School Engineering and Applied Sciences. He holds 26 US and 13 international patents (licensed to 25 companies), is a founder of VirtualScopics, and has published 250+ journal articles. He is a fellow of the IEEE, AIUM, ASA, AIMBE, and NAI.

Sedigheh S. Poul received her BS degree from the University of Tehran, Iran, in 2014 and her MS degree from the University of Rochester in August 2019, both in mechanical engineering. She is a PhD student in the Department of Mechanical Engineering at the University of Rochester. Her research interests include ultrasound elastography, tissue characterization, viscoelasticity, and finite-element modeling.